Catalysis Science & Technology

ROYAL SOCIETY OF CHEMISTRY

PAPER

Published on 08 July 2026
Licence and permissions

Cite this: DOI: 10.1039/d6cy00157b

Chromium oxide/nitride-decorated nitrogen-doped reduced graphene oxide as an efficient oxygen reduction electrocatalyst for alkaline zinc–air batteries

Amin Balavandi,[a] Aso Navaee,[a] Ali Feizabadi,[b] Rezgar Ahmadi, [ac] Katayoon Gholami Laelabadi[a] and Abdollah Salimi [*ac]

Advancements in zinc–air batteries critically depend on the development of sustainable, high-efficiency electrocatalysts for the oxygen reduction reaction (ORR). In this work, we report a chromium oxide/hydroxide/nitride/carbon@nitrogen-doped reduced graphene oxide nanocomposite (NRGO–N–CrO(OH)–C) as an effective ORR electrocatalyst in alkaline media. Nitrogen-doped reduced graphene oxide (NRGO) was synthesized *via* an electrochemical method, while chromium oxide–carbon (Cr_2O_3–C) was prepared using a facile soft-template approach. Subsequent deposition of Cr_2O_3–C onto NRGO and *in situ* formation of CrOH/N were achieved through a hydrothermal process. The structural and morphological characteristics of the NRGO–N–CrO(OH)–C nanocomposite were systematically investigated using various microscopy and spectroscopy techniques, confirming the uniform distribution of resulted Cr-based nanostructures on the NRGO sheets. Electrochemical studies demonstrate outstanding ORR activity and durability, with an onset potential of 0.86 V and a half-wave potential of 0.715 V *versus* RHE, and rotating disk electrode measurements reveal a dominant four-electron ORR pathway. When employed as an air cathode in zinc–air batteries, the NRGO–N–CrO(OH)–C catalyst delivers superior performance compared to commercial noble-metal catalysts, achieving a high open-circuit voltage of 1.48 V, a specific capacity of 665 mA h g^{-1} and a peak power density of 156 mW cm^{-2}, surpassing the commercial Pt/C catalyst, which has a power density of 134 mW cm^{-2}. Remarkably, the battery exhibits a satisfactory long-term cycling stability over 1680 cycles (280 h) with a coulombic efficiency of 63.8%. These results highlight the NRGO–N–CrO(OH)–C nanocomposite as a cost-effective and high-performance ORR electrocatalyst, offering a promising pathway for advanced zinc–air battery technologies.

Received 6th February 2026,
Accepted 4th July 2026

DOI: 10.1039/d6cy00157b

rsc.li/catalysis

1. Introduction

In the pursuit of sustainable energy solutions, the landscape of modern energy research has increasingly shifted focus towards cutting-edge energy conversion and storage technologies, notably fuel cells and metal–air rechargeable batteries. These innovations are pivotal in our transition towards renewable energy, especially with metal–air batteries emerging as a key player due to their efficient, sustainable, and cost-effective power generation. Utilizing metals like zinc, magnesium, and aluminum as anodes, and air electrodes that capture atmospheric oxygen, these batteries offer unparalleled specific energy and environmental benefits, making them suitable for a wide range of applications, from primary power sources to emergency backup systems. However, key obstacles, including the substantial overpotential needed for the oxygen evolution reaction (OER) while charging and the sluggish kinetics of the oxygen reduction reaction (ORR) when discharging, considerably hinder their progression.[1]

Addressing these challenges, extensive research has been directed towards developing cost-effective and high-performance catalysts for the ORR, traditionally relying on noble metals like platinum, palladium, and ruthenium for their excellent catalytic properties. However, the scarcity and high cost of these metals demand alternatives, prompting researchers to explore strategies to reduce reliance on these precious metals.[2] Innovations include alloying noble metals with abundant transition metals,[3–5] incorporating non-metallic elements into carbon matrices,[6–8] and designing complex carbon substrates integrated with

[a] Department of Chemistry, University of Kurdistan, Sanandaj, 66177-15175, Iran. E-mail: absalimi@uok.ac.ir; Tel: +989188710673
[b] Department of Chemistry, University of Western Ontario, London, ON, Canada
[c] Research Center for Nanotechnology, University of Kurdistan, Sanandaj, 66177-15175, Iran

metal and non-metallic elements to enhance ORR activity and durability.[9,10] Among these, metal oxides, particularly Mn_2O_3, NiO, CoO, and $LiCoO_2$, have shown promise as viable alternatives to platinum-based catalysts due to their abundance, low cost, and high stability.[11–19]

Further advancements in the field have highlighted the potential of chromium oxides and graphene-supported metal oxides as efficient catalysts. Despite the poor conductivity of chromium oxide, its combination with carbon materials such as graphene, known for its excellent electronic conductivity, has shown significant promise for ORR applications. Building upon these findings, this study introduces an innovative approach utilizing nitrogen-doped reduced graphene oxide (NRGO) with chromium oxide containing carbon (Cr_xO_y–C) as an electrocatalyst in zinc–air batteries (ZABs). This exploration is further enriched by addressing the inherent challenge on natural inertness of graphene oxide towards the ORR. Its modified form, reduced graphene oxide (RGO), showcases considerable promise due to its high electrical conductivity. However, the presence of abundant oxygen-containing groups in GO enables extensive chemical and physical modifications, thereby enhancing ORR efficiency after converting to modified RGO and reaching a viable option for catalytic improvement in ZABs.[20–22] The strategic incorporation of nitrogen doping plays a crucial role in this context. Nitrogen doping has been recognized for its significant ability to alter the electronic and geometric properties of carbon lattices, thus enhancing the electrocatalytic activity of carbonaceous materials like RGO for the ORR and other reactions.[9,23,24] This modification contributes to the superior performance of nanocomposites between NRGO and Cr_xO_y–C.[25,26]

Chromium(III) oxide (Cr_2O_3) is receiving significant attention as a novel anode material due to some of its unique characteristics such as a high theoretical capacity of 1058 mA h g^{-1} and a comparatively low lithium insertion voltage of 1.085 V. One major advantage of using Cr_2O_3 as an electrode material for LIBs is the fundamental process of charge storage in this system, which is based on the conversion reaction, displaying much higher energy density than the conventional electrode materials.[27–30] On the other hand, Cr_2O_3-based nanomaterials have been used for modification of cathode electrodes in energy conversion devices such as zinc–air batteries, thus different nanomaterials of Cr_2O_3 with high electrocatalytic activity have been used as electrocatalysts for the oxygen reduction reaction.[31,32] Although the application of Cr_xO_y based nanomaterials for the oxygen reduction reaction (ORR) has been reported, the observed overpotential and calculated Tafel slope are not adequately suitable for large-scale industrial implementation. Thus, synthesis of Cr_xO_y based nanomaterials with lowered overpotentials and decreased Tafel slopes is a challenge.[31–34]

In this study, chromium oxide is prepared, assisted by urea and oxalic acid under hydrothermal conditions followed by thermal annealing, according to previously reported work in the literature.[25] At the same time, choline chloride/urea is used as a nitrogen precursor for synthesis of NRGO as a platform for decoration of Cr_2O_3–C nanoparticles. Through this decoration the synergistic effect of the resulted composite improved catalytic activity toward ORR compared to NRGO and Cr_2O_3–C separately. The selection of Cr_2O_3–C as the primary oxide component is motivated by its high chemical stability in alkaline media, corrosion resistance, and favorable electronic configuration. The partially filled 3d orbitals of Cr^{3+} can contribute to oxygen adsorption and intermediate stabilization during the ORR. In addition, the partial nitridation to CrN and the interaction with nitrogen-doped graphene may further optimize the electronic structure and enhance charge transfer through synergistic effects.

The breakthroughs are evidenced by superior onset potential and durability comparable to commercial platinum catalysts, marks a significant step forward in the development of efficient, stable, and sustainable rechargeable ZABs, aligning with the global pursuit of green energy solutions for the 21st century.[35,36] After characterization, the proposed nanocomposite is demonstrated as NRGO–N–CrO(OH)–C, showing low charge transfer resistance, decreased onset potential and a small Tafel slope for the ORR. After that, it is utilized as a cathode in a Zn–air battery (ZAB), which displayed a high open-circuit voltage of 1.48 V and a power density of 156 mW cm^{-2}, and surpassed the commercial Pt/C catalyst, which has a power density of 134 mW cm^{-2}.

2. Experimental

2.1. Materials and analytical techniques

Chemicals such as graphite rods (purity of 99.9%), urea, choline chloride (purity ≥ 99%), oxalic acid (anhydrous for synthesis), polyethylene glycol (PEG, Mw = 200), ethanol (purity of 99.6%), and chromium nitrate nonahydrate ($Cr(NO_3)_3{\cdot}9H_2O$, 99%) were sourced from Merck and Sigma-Aldrich Co. and utilized as received without any additional purification. The structural details of the synthesized nanostructures were characterized using a field-emission scanning electron microscope (FE-SEM, model MIRA3 FEG-SEM by TESCAN, Czech Republic) at 20 kV, equipped with an energy dispersive spectrometer (EDS), along with a transmission electron microscope (TEM, model EM 208S). The phase compositions were analyzed *via* X-ray diffraction (XRD) using a Philips EXPERTMPD diffractometer, employing Ni-filtered Cu Kα radiation (λ = 0.154 nm). Surface chemical compositions were examined by X-ray photoelectron spectroscopy (XPS) on a Kratos AXIS Supra spectrometer using a monochromatic Al Kα source (15 mA, 15 kV). Fourier transform-infrared (FT-IR) spectra (range 4000–400 cm^{-1}) were recorded using a BRUKER Vector-22 spectrophotometer (Switzerland), employing the KBr pellet method at ambient temperature, and Raman spectroscopic analysis was conducted with a Horiba LabRAM ARAMIS

spectrometer using a 514 nm Ar ion continuous wave (CW) laser.

To investigate the stability of the Cr-based nanostructure in the resulting composite, the electrolyte solution used for the ORR after 2 and 4 hours was preserved and atomic adsorption spectroscopy using a VARIAN SpecrAA 220 equipped with an electrical furnace, which detects ppb amounts of metals, was performed to detect the possible existing Cr^{n+} species in the electrolyte.

2.2. Preparation of Cr_2O_3–C

The synthesis of Cr_2O_3-based composites commenced with the dissolution of 0.35 g of oxalic acid in a mixture of 21 mL of polyethylene glycol (PEG, Mw = 200) and 7 mL of ethanol, ensuring complete dissolution of the oxalic acid. Subsequently, 0.45 g of urea and 0.8 g of $Cr(NO_3)_3{\cdot}9H_2O$ were sequentially introduced to the solution. This resulting mixture was then transferred to a 40 mL Teflon-lined autoclave, which was securely sealed and subjected to a temperature of 180 °C for 5 h to ensure complete dissolution of all components. Following this, the formed precipitate was collected and washed with ethanol. The final step involved annealing the collected product in a quartz tube at 750 °C for 6 h under an argon atmosphere and subsequently at 500 °C for 2 h in air, yielding Cr_2O_3–C nanostructures.[25]

2.3. Synthesis of NRGO

For synthesis of NRGO, two graphite rods were utilized as both anode and cathode, set in about 1 cm apart from each other within a solution containing ionic liquids to assist the electrochemical exfoliation process.[7] The process began by formulating an electrolyte solution, achieved by blending choline chloride and urea in a 1 : 2 molar ratio with adding adequate deionized water, and then almost all of the water was removed from the mixture during heating at 70 °C. The resulting mixture acted as the ionic liquid medium required for graphite exfoliation. To kickstart the exfoliation, a direct current (DC) as much as 5 V was applied.[37] The presence of urea in the solution provides nitrogen source for doping, crucial for enhancing the characteristics of the final NRGO product. Upon completion of the exfoliation, the resulting graphene was gathered using a membrane filter and was extensively rinsed with deionized water to ensure the elimination of any remaining impurities.

2.4. Preparation of the NRGO–N–CrO(OH)–C catalyst

Following the synthesis of Cr_2O_3–C nanostructures and the creation of NRGO *via* electrochemical exfoliation, the next step involved the preparation of nitrogen-doped reduced graphene oxide-supported Cr_2O_3–C nanostructures using a hydrothermal method. This process began by dispersing 0.02 g of the previously prepared Cr_2O_3–C nanomaterial in 70 mL of NRGO dispersion (1.0 mg mL^{-1}). The mixture was subjected to ultrasonication to ensure even distribution of the nano compounds within the NRGO dispersion. Following an hour of ultrasonication, 0.1 g of urea was added to the solution to facilitate nitrogen doping during the hydrothermal reaction. The mixture was then transferred into a 100 mL Teflon-lined autoclave, sealed with a Teflon lid to ensure containment, and heated at 120 °C for two hours. Upon completion of the hydrothermal process, a black precipitate was obtained. This precipitate was thoroughly filtered, washed with ultrapure water to remove any residual reactants, and dried for 12 h at 60 °C, resulting in the formation of the NRGO–N–CrO(OH)–C nanocomposite.[38] This synthesis pathway is schematically represented in Fig. 1 to provide a clear overview of the process and the interactions involved in producing the NRGO–N–CrO(OH)–C composites. In order to investigate the effect of the hydrothermal procedure, a physical mixture of synthesized NRGO and Cr_2O_3–C without hydrothermal conditions was also prepared and used as an electrocatalyst.

2.5. Electrochemical characterization

Electrochemical analyses for all samples were conducted using an AUTOLAB modular electrochemical system (ECO Chemie, The Netherlands), equipped with a PGSTAT type III unit, and operated *via* NOVA software. A standard three-electrode setup was employed, comprising a platinum rod counter electrode, an Ag/AgCl (saturated KCl) reference electrode, and a glassy carbon electrode (GCE) with a 2 mm diameter serving as the working electrode, immersed in a 0.5 M aqueous KOH solution as the electrolyte. Catalyst ink was prepared by ultrasonically dispersing the synthesized materials in isopropyl alcohol with 0.5 wt% Nafion for 10 minutes. The catalyst ink was then applied to the GCE surface using a drop-drying technique and left to dry at room temperature. To standardize potentials, all readings taken with the Ag/AgCl electrode were converted to the reversible hydrogen electrode (RHE) scale using the formula $E_{RHE} = E_{Ag/AgCl} + 0.059\ pH + E^{\circ}_{Ag/AgCl}$, where $E_{Ag/AgCl}$ is the measured potential and $E^{\circ}_{Ag/AgCl} = 0.197$ V. The electrochemical surface area (ECSA) of the catalyst materials was obtained using the double-layer capacitance (DLC) obtained from cyclic voltammograms recorded in the non-redox region of the electrodes in 1.0 M KOH solution. The ECSA value can be calculated using the following equation.

$$ECSA = C_{dl}/C_s \quad (1)$$

where C_{dl} is the DLC, which depends on the slope of the current *vs.* scan rate plot. C_s is the standard specific electrochemical DLC and its value for 1 M KOH electrolyte is 40 μF cm^{-2} based on a previous report.[26] Electrochemical parameters such as onset potential (at 0.001 mA cm^{-2}) and half-potential (at half of highest diffusion limited current density) obtained from the RDE voltammetric measurements for the ORR in oxygen-saturated 0.5 M KOH solution at a rotation speed of 1600 rpm.

2.6. Zinc–air battery performance assessment

The air cathode (total thickness = 1.5 mm) is composed of carbon paper with activated carbon dispersed in a mixed

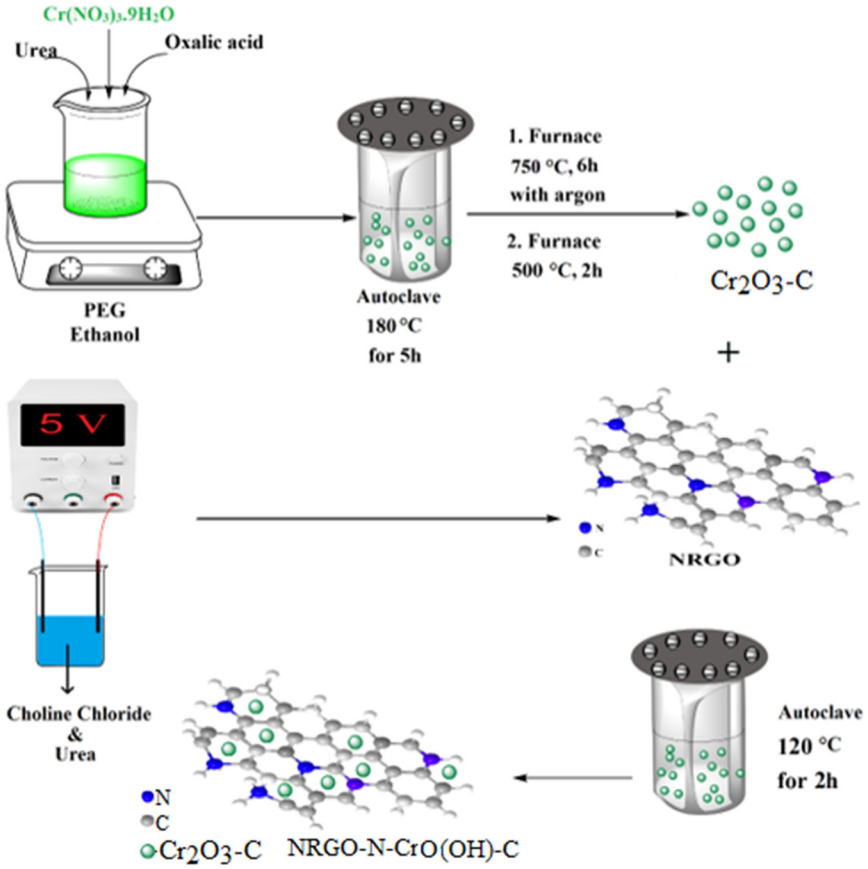

Fig. 1 Schematic of the synthesis process of the NRGO–N–CrO(OH)–C nanocomposite.

solution of 100 μl of ethanol and 10 μl of PTFE (40 wt%) and electrocatalyst ink. This setup includes nickel foam as the cathodic current collector and carbon felt as a gas diffusion layer (GDL), which prevents electrolyte leakage, while allowing oxygen from atmospheric air to enter the cell. The anode consists of Zn powder and Cu foam as the anodic current collector, with 6.0 M KOH solution containing 0.2 M $Zn(OAC)_2$ as the electrolyte. The galvanostatic discharge and charge cycling of the Zn–air batteries was performed at a current density of 2 mA cm^{-2}, which each cycle lasting 10 minutes (5 minutes for charging and 5 minutes for discharging). To benchmark the effectiveness of the developed catalyst, a control electrode coated with 10 wt% Pt/C on carbon paper, with a mass loading of 10 mg cm^{-2}, was utilized as the air cathode. Electrochemical evaluations were carried out using a custom-built Zn–air battery setup.

3. Results and discussion

3.1. Structure characterization of the catalysts

The structural characteristics and surface morphology of Cr_2O_3–C and NRGO–N–CrO(OH)–C nanocomposites were thoroughly examined using scanning electron microscopy (SEM) and transmission electron microscopy (TEM) techniques. SEM images (Fig. 2(A–C)) reveal the distinct morphologies of NRGO and Cr_2O_3–C nanostructures and the combination of both structures, respectively. NRGO displays a sheet-like structure with a rough surface, indicating well-exfoliated graphene sheets with thicknesses ranging from 5–10 nm. Fig. 2B shows the nanostructured Cr_2O_3–C, calcined at 500 °C, presenting a flower-like morphology consisting of spherical-shaped nanoparticles aligning in a cylinder-like form with an average width size of 57 nm. The images highlight the tendency of the resulting Cr-based catalyst to form agglomerated structures due to the small particle size and the influence of London–van der Waals forces and maybe magnetic properties on the surface of nanoparticles, facilitating the aggregation into larger particles. Fig. 2(C) demonstrates the SEM image of the NRGO–N–CrO(OH)–C composite. As can be seen, the surface of NRGO sheets displays more roughness than NRGO sheets due to deposition of Cr-based nanoparticles on graphene sheets, thus the presence of NRGO effectively restricted the aggregation of Cr-based nanostructures through anchoring on the surface of nitrogen-functionalized graphene oxide sheets. Fig. 2(D) shows a typical TEM image of the NRGO–N–CrO(OH)–C catalyst and the corresponding histogram of particle size distribution. It can be seen that under final hydrothermal conditions, Cr-based nanostructures uniformly distributed on NRGO nanosheets with an average particle size of 39.0 nm estimated from the histogram profile (inset of Fig. 2(D)), thus the results

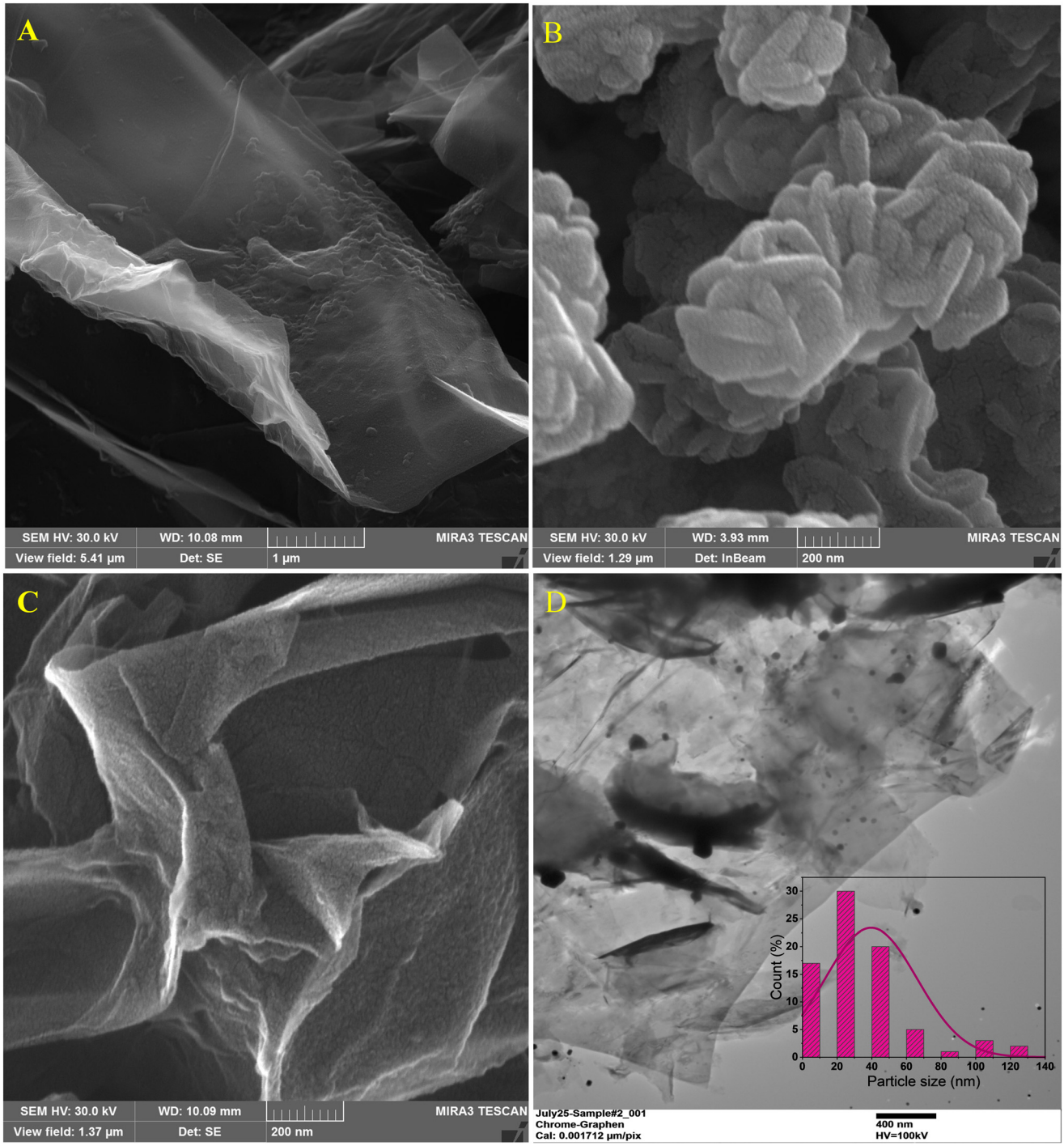

Fig. 2 SEM images of (A) NRGO, (B) Cr_2O_3–C, and (C) NRGO–N–CrO(OH)–C. (D) TEM image and the corresponding particle size distribution histogram (inset) of NRGO–N–CrO(OH)–C.

confirmed the successful synthesis of the intended composites. To further elucidate the structural features of the catalyst, higher-magnification TEM images (Fig. S7, SI) were included. The images clearly show the uniform dispersion of chromium-based nanoparticles on the NRGO sheets, with small particle sizes and strong anchoring onto the nitrogen-doped graphene support. Such homogeneous distribution and intimate interfacial contact can expose active sites and facilitate efficient electron transfer during catalytic applications.

Energy-dispersive X-ray (EDX) spectroscopy further corroborates the composition of these materials; the corresponding EDX elemental mapping reveals a uniform distribution of carbon, nitrogen, and oxygen elements in the NRGO, Cr_2O_3–C, and NRGO–N–CrO(OH)–C composites (Fig. S1–S3).

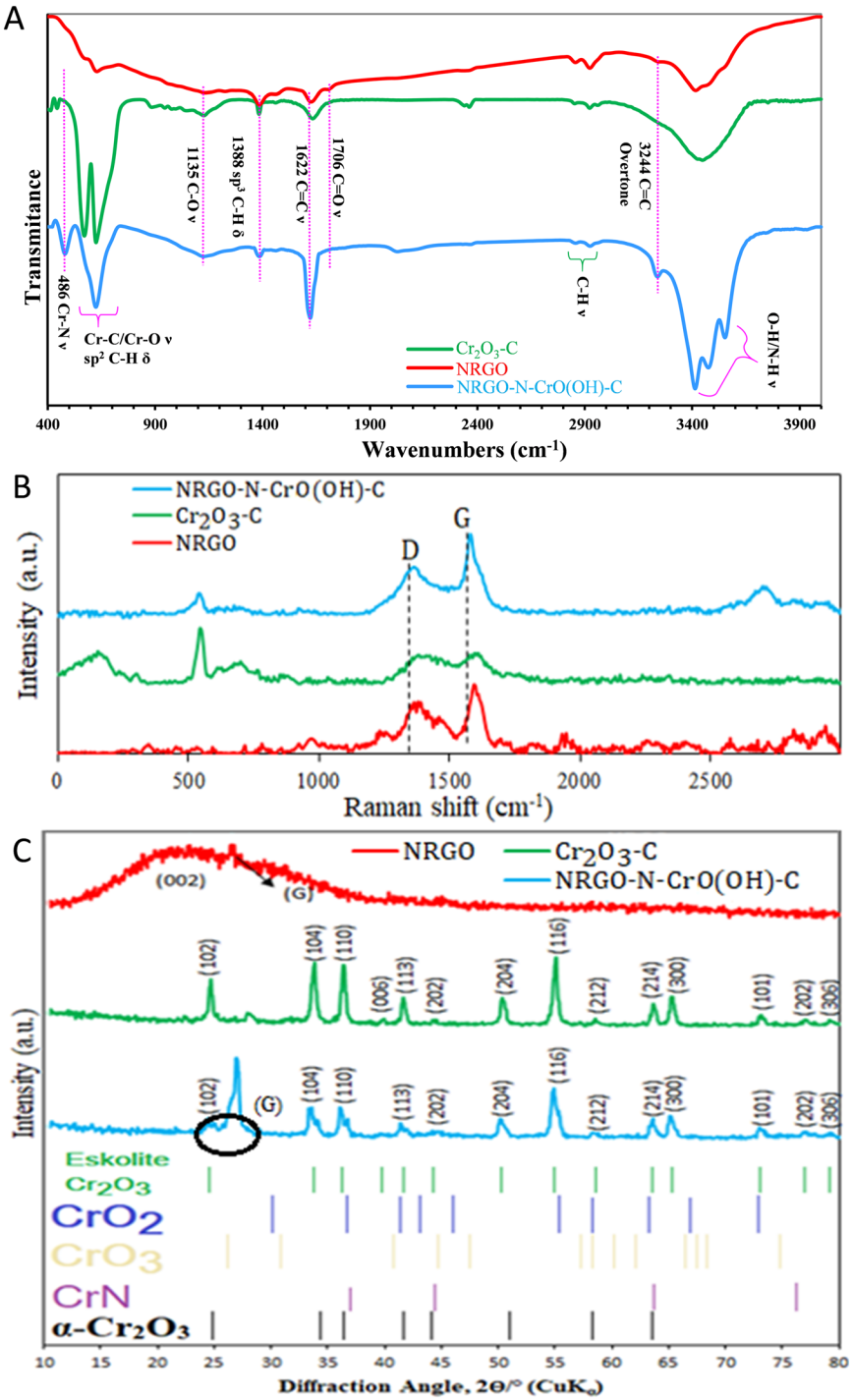

Fig. 3 (A) FTIR spectra, (B) Raman spectra, and (C) XRD patterns of NRGO, Cr_2O_3–C, and NRGO–N–CrO(OH)–C.

The FTIR spectra of all three materials are presented in Fig. 3A. Compared to NRGO, for the case of Cr_2O_3–C two intense peaks at 572 and 630 cm^{-1} are observed, which can be attributed to the Cr–O (ref. 27) or Cr–C stretching vibrations. But for the case of NRGO–N–CrO(OH)–C, the intensities of these peaks, especially at 572 cm^{-1}, are decreased, while another peak at 486 cm^{-1} appears, possibly owing to the conversion of Cr–O or Cr–C bonds to C–N bonds. The FTIR peak at 624 cm^{-1} for NRGO can be attributed to sp^2 C–H bending. For the case of Cr_2O_3–C, an intense peak broadened from 3330 to 3650 assigned to O–H stretching vibration is observed, while in the cases of NRGO and NRGO–N–CrO(OH)–C, this peak is overlapped with two N–H stretching vibration peaks, confirming the existence of amine functional groups in the resulting composite. The location and related vibration (ν)/bending (δ) values of other

important peaks are assigned on the same Figure. The overall FTIR analysis strongly confirms the successful synthesis of the proposed composite.

Raman spectroscopy was utilized to analyze the short-range structural order within NRGO, Cr_2O_3–C, and their combined NRGO–N–CrO(OH)–C nanocomposite. The observed peak at approximately 550 cm^{-1} in Fig. 3B is observed in both pure Cr_2O_3–C and the composite material, resulting from the Cr–O lattice vibrations. In the spectra of NRGO, Cr_2O_3–C, and the NRGO–N–CrO(OH)–C composite, two prominent peaks are evident, corresponding to the D band (indicative of disordered carbon structures) and the G band (representing graphitic carbon). Previous studies have shown that the ratio of the D to G bands (I_D/I_G) is inversely related to the size of the in-plane crystallites (L_a).[39] This relationship is quantified by the Tuinstra–Koenig (T–K) equation, L_a (nm) = $(2.4 \times 10^{-10})\lambda^4(I_D/I_G)^{-1}$, where λ denotes the wavelength of Raman excitation.[32,33] Analysis of the crystallite sizes in NRGO *versus* NRGO–N–CrO(OH)–C reveals I_D/I_G ratios of 0.77 and 0.59, corresponding to crystallite sizes of 21.76 nm and 28.39 nm, respectively. This indicates an increase in crystallite size upon the integration of Cr_2O_3–C into the NRGO matrix, which may result from the deposition of nanoparticles with the form of CrO(OH)–C on the surface of NRGO as a support without violently damaging the carbon crystal structure and probable formation of N–Cr bonds through amine functional groups of NRGO.

The X-ray diffraction (XRD) analysis of Cr_2O_3–C nanoparticles was performed over a continuous scanning range from 10° to 80°, using a current of 30 mA and a voltage of 40 kV, along with Ni-filtered Cu-Kα radiation, as depicted in Fig. 3C. The observed diffraction peaks for both the pure Cr_2O_3–C and the NRGO–N–CrO(OH)–C composite are indicative of the (102), (104), (110), (006), (113), (202), (204), (116), (212), (214), (300), (1010), (220), and (306) planes, characterizing the hexagonal structure of well-crystallized Cr_2O_3–C (with the space group $R\bar{3}c$ and lattice parameters a = 4.961 Å, b = 4.961 Å, and c = 13.599 Å). The XRD patterns further verify that the synthesized nanoparticles consist exclusively of the eskolaite phase of Cr_2O_3–C ($Cr_{12}O_{18}$) and α-Cr_2O_3,[40,41] clearly indicating the absence of other chromium oxide phases like CrO_2 and CrO_3.[32,34,35] However, as can be seen in the XRD pattern of NRGO–N–CrO(OH)–C, an additional intense peak at 2θ of 27° appears, which can be assigned to $Cr(OH)_3$. Moreover, diffraction peaks as shoulder peaks or with weak intensity located at 2θ values of 37.5, 43.7, 63.4, and 76.3° are assigned to the (111), (200), (220), and (311) planes, respectively, characteristic of the cubic-phase crystallographic structure of CrN.[28] Therefore, the appearance of these peaks can indicate that some of the Cr–O bonds in the Cr_2O_3–C crystals probably converted to Cr(OH) and CrN during the hydrothermal process.

The average crystallite size of Cr_2O_3–C as well as N–CrO(OH) in the NRGO–N–CrO(OH)–C composite was estimated from the Scherrer formula by using the full width at half maximum (FWHM) of the Cr_2O_3 (116) diffraction peak at 2θ ~ 55°, which has a higher intensity and is a completely isolated peak from the NRGO as well as other Cr_2O_3–C diffraction peaks. Compared to the Cr_2O_3–C nanostructure, the slight expansion of peaks in the NRGO–N–CrO(OH)–C sample indicates that after composite formation, the crystallinity of Cr-Based nanostructures is decreased, where the average crystallite sizes of Cr_2O_3 in two samples are 26.0 and 30.4 nm, respectively. This phenomenon may be because of formation of Cr(OH) and CrN on the surface of Cr_2O_3 nanostructures.

Elemental analysis and oxidation state analysis of elements were further performed using XPS to obtain information about the interaction of Cr_2O_3 nanoparticles with NRGO. Notably, Fig. 4A displays the survey scan, with prominent peaks at 576.9, 586.7, 531.0, 284.8, and 399.3 eV, attributed to the electronic states of Cr $2p_{3/2}$, Cr $2p_{1/2}$, O 1s, C 1s, and N 1s, respectively,[24,36,37] as also detected by the EDX study. The atomic percentages of C, O, N and Cr are obtained to be 76.66, 15.66, 3.30 and 4.38, respectively.

Deconvolution of XPS narrow scans for each element reveals the electronic status and results are summarized in Table 1. For the case of Cr 2p (Fig. 4B) chromium combined with carbon, oxygen and nitrogen are identified, in which about ~15% Cr combined with C, ~35% Cr combined with nitrogen and ~0.35% Cr–OH are observed, indicating the interaction between some of the Cr_2O_3 at the surface of the crystal with amine and water during the hydrothermal procedure. Deconvolution of the C 1s, N 1s and O 1s spectra, shown in Fig. 4C–E, also confirm the existing of Cr–C, Cr–N and Cr–O, respectively. Moreover, the other deconvoluted peaks from the N 1s spectrum in Fig. 4E reveal the probable existence of N═C, N–C, N–H and N–O/N═O bonds in the resulting composite. In addition, there is a very small amount of C–O/C═O or N–O/N═O, confirming obtaining reduced graphene oxide during functionalization by nitrogen.

3.2. Electrocatalytic performance of the catalysts

Cyclic voltammetry (CV) analysis was conducted to evaluate the electrocatalytic performance of the catalysts towards the ORR. CV profiles for NRGO, Cr_2O_3–C, NRGO–N–CrO(OH)–C, and Pt/C were recorded in O_2-saturated 0.5 M KOH solution at a scan rate of 5 mV s^{-1}, with a comparison of these profiles shown in S4A. Linear sweep voltammetry (LSV) measurements for the ORR on NRGO, Cr_2O_3–C, NRGO–N–Cr_xO_y(OH)–C, physically mixed NRGO + Cr_2O_3–C without a nitridation step and Pt/C in 0.5 M KOH solution, performed under O_2 saturation at a scan rate of 5 mV s^{-1}, are depicted in Fig. 5A. Among these, the NRGO–N–CrO(OH)–C composite shows superior catalytic efficiency for the ORR compared to the other tested electrocatalysts under identical experimental conditions. NRGO–N–CrO(OH)–C demonstrated improved ORR activity compared to pure NRGO, evidenced by a more positive onset potential of 860 mV (165 mV higher than NRGO), indicating faster ORR kinetics due to improved electron conductivity. The cathodic peak observed at ~0.75 V

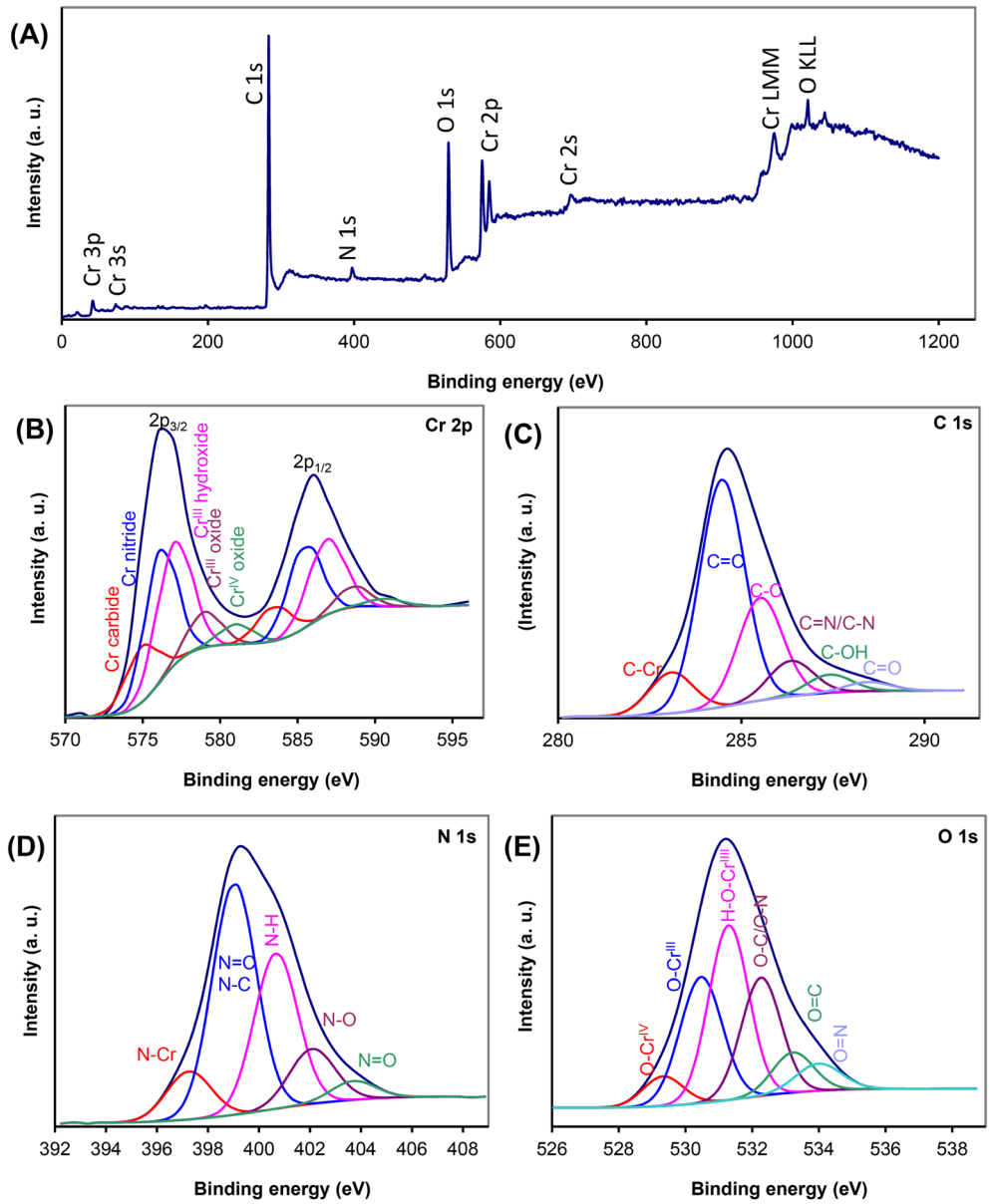

Fig. 4 (A) Full X-ray photoelectron spectroscopy (XPS) spectra of NRGO–N–CrO(OH)–C and high-resolution XPS spectra of (B) Cr2p, (C) O 1s, (D) C 1s, and (E) N 1s.

Table 1 Possible compound types resulting from XPS deconvolution of the narrow scan of existing atoms in the NRGO–N–CrO(OH)–C composite

XPS peak	Possible compound types and related binding energies					
C 1s	C–Cr 283.2	C═C 284.4	C–C 285.7	C–N, C═N 286.4	C–OH 287.5	288.5 C═O
N 1s	N–Cr 297.4	N═C, N–C 399.2	N–H 400.6	N–O 401.9	N═O 403.7	
O 1s	O–Cr^{IV} 529.4	O–Cr^{III} 530.6	HO–Cr^{III} 531.4	O–C, O–N 532.3	O═C 533.3	O═N 534.0
Cr $2p_{3/2}$	Cr–C 574.9 (~15%)	Cr–N 576.2 (~35%)	Cr^{III}–OH 577.1	Cr^{III}–O 579.0	Cr^{IV}–O 581.0	

in the CV curves is associated with the oxygen reduction process occurring on the catalyst surface. This phenomenon is commonly attributed to the initial adsorption and reduction of oxygen molecules on the active sites of the catalyst, leading to the formation of intermediate species (*e.g.*, O_2^- or OOH*) during the ORR process in alkaline media. In the present catalyst, these processes are likely facilitated by the nitrogen-doped carbon framework together with chromium-based active sites (Cr–N environments).

By integrating results from rotating disk electrode (RDE) experiments and Tafel analysis, the relationship between kinetic parameters and the influence of anions on the ORR

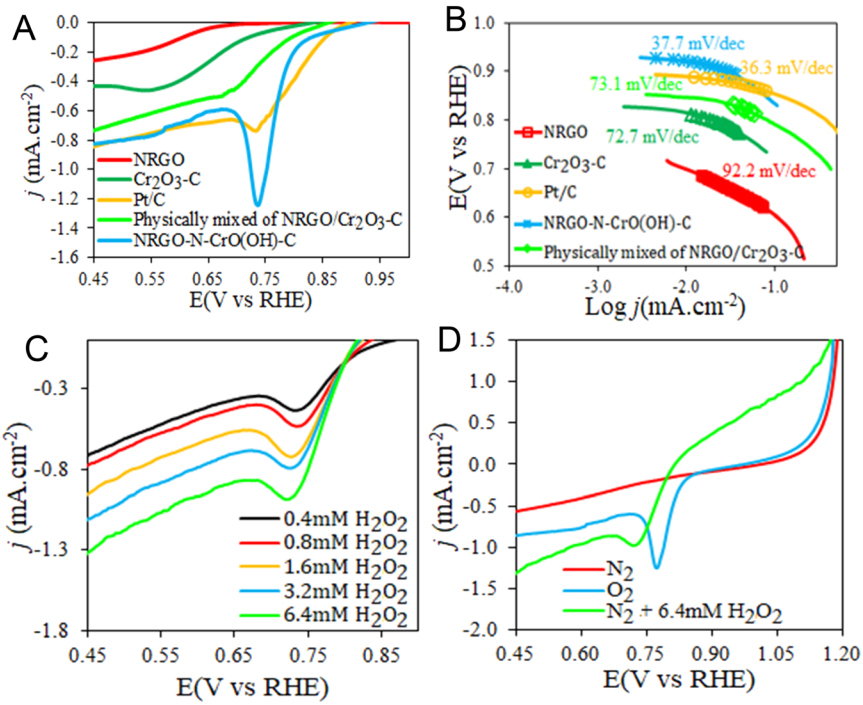

Fig. 5 (A) Linear sweep voltammetry (LSV) curves for the oxygen reduction reaction (ORR) and (B) Tafel slopes of NRGO, Cr_2O_3–C, NRGO–N–CrO(OH)–C, physically mixed NRGO + Cr_2O_3–C without a hydrothermal nitridation step and Pt/C in 0.5 M of KOH solution at a scan rate of 5 mV s^{-1} on glassy carbon. (C) Voltammograms obtained in N_2-purged 0.5 M KOH solutions with various concentrations of H_2O_2 at a scan rate of 5 mV s^{-1} for NRGO–N–CrO(OH)–C, compared to (D) voltammograms in O_2-purged and N_2-purged solutions + 6.4 mM H_2O_2 in 0.5 M KOH on glassy carbon.

can be determined. The polarization curves plotted in Fig. 5B (against RHE) *versus* $\log i$, referred to as Tafel plots, are derived from the following Tafel equations:

$$\eta = b \log \frac{i}{i_0} \quad \text{where } b = \frac{2.3RT}{(1-\alpha)nF} \tag{2}$$

Tafel analysis showed that NRGO–N–CrO(OH)–C exhibits a significantly reduced Tafel slope of 37.7 mV dec^{-1}, in contrast to 72.7 mV dec^{-1} for Cr_2O_3–C, 73.1 mV dec^{-1} for physically mixed NRGO + Cr_2O_3–C and 92.2 mV/dec for NRGO, while presenting a Tafel slope comparable to that of Pt/C, which is 36.3 mV dec^{-1}, as depicted in Fig. 5B. This indicates faster kinetic reactions for NRGO–N–CrO(OH)–C than for the other two materials alone. Fig. 5C examines the electrocatalytic activity of the NRGO–N–CrO(OH)–C catalyst toward hydrogen peroxide reduction. As illustrated, the modified electrode shows excellent activity for hydrogen peroxide reduction, and cathodic currents increased with increasing H_2O_2 concentrations (Fig. 5D). These results indicate that NRGO–N–CrO(OH)–C exhibits electrocatalytic activity for both oxygen and hydrogen peroxide reduction, which confirms 4e reduction of oxygen.

LSV measurements, which were conducted from 1.2 to 0.0 V (*vs.* RHE) at rotation speeds from 200 to 1600 rpm, and Koutecky–Levich (K–L) results for NRGO–N–CrO(OH)–C in O_2-saturated 0.5 M KOH solution are shown in Fig. 6A and B. The limiting current densities, as shown in Fig. 6A, appear at higher overpotentials across higher rotation speeds. Additionally, a positive linear relationship between the current density and rotation rate is observed in both the mixed control zone and the diffusion control region, as indicated in Fig. 6A. This behavior of the NRGO–N–CrO(OH)–C electrocatalyst allows for the detailed examination of the ORR kinetics.

The K–L curve demonstrates clear linear and parallel trends between 0.50 V and 0.65 V, as illustrated in Fig. 6B. This indicates that the electron transfer numbers for the NRGO–N–CrO(OH)–C electrocatalyst vary across different polarization potentials during the ORR. Kinetic details of the oxygen reduction process for varying rotation speeds are detailed in Fig. 6B.

The K–L equation was employed to determine the electron transfer number obtained from LSV of the NRGO–N–CrO(OH)–C modified electrode at different rotation speeds.[55]

$$\frac{1}{j} = \frac{1}{j_k} + \frac{1}{j_d} = \frac{1}{nFkC_0} + \frac{1}{0.62nFD_{O_2}^{2/3}\upsilon^{-1/6}C_0\omega^{1/2}} \tag{3}$$

j: current density, A cm^{-2}; j_k: kinetic current density, A cm^{-2}; j_d: diffusion-limited current density, A cm^{-2}; n: the number of electrons transferred per molecule of O_2 in the ORR; F: Faraday's constant, 96 485 C mol^{-1}; k: the rate constant for O_2 reduction; D_{O_2}: diffusion coefficient of O_2 in 0.5 M KOH, 1.65×10^{-5} cm^2 s^{-1}; υ: kinematic viscosity of the 0.5 M KOH electrolyte, 1.0×10^{-2} cm^2 s^{-1};[54,56] C_0: saturated concentration of O_2 in 0.5 M KOH at 1 atm O_2 pressure,

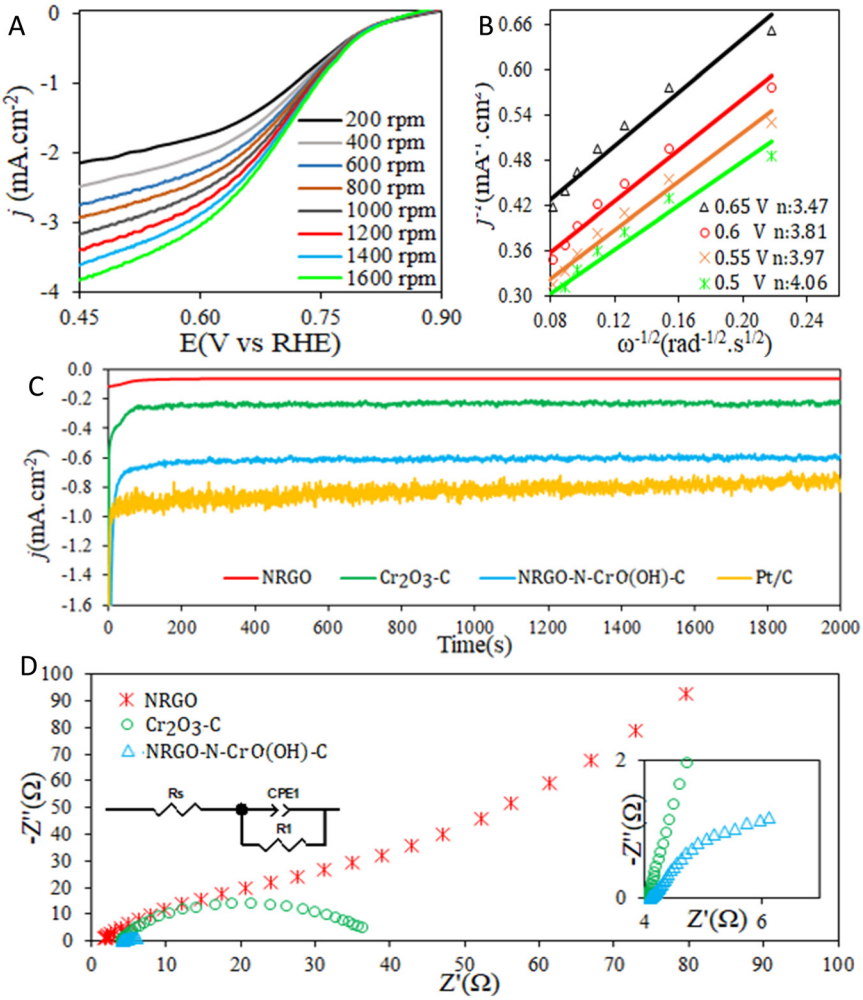

Fig. 6 (A) Rotating-disk voltammograms for NRGO–N–CrO(OH)–C in O_2-saturated 0.5 M KOH solution at different rotation speeds (scan rate of 5 mV s^{-1}). (B) Corresponding Koutecky–Levich plots for NRGO–N–CrO(OH)–C at potentials of 0.5 V, 0.55 V, 0.6 V, and 0.65 V *vs.* RHE on glassy carbon electrodes. (C) Chronoamperometric response of the NRGO–Cr_2O_3–CrN–C electrocatalyst for the oxygen reduction reaction (ORR) at 0.5 V *vs.* RHE in O_2-saturated 0.5 M aqueous KOH solution on glassy carbon. (D) Electrochemical impedance spectra of NRGO, Cr_2O_3–C, and NRGO–N–CrO(OH)–C on glassy carbon electrodes at a fixed potential of 0.8 V *vs.* RHE in O_2-saturated 0.5 M KOH. The inset of D represents the higher magnification at low *Z* values.

1.0×10^{-6} mol cm^{-3}; ω: rotation rate, rad s^{-1}. The number of electrons transferred (n) during the ORR using the NRGO–N–CrO_y(OH)–C electrocatalyst is approximately 4, as shown in Fig. 6B based on the plot of $1/j$ *vs.* $\omega^{-1/2}$. This indicates that the ORR mechanism with NRGO–N–CrO(OH)–C follows a 4-electron pathway, specifically the direct reduction of O_2 to OH^-, within the diffusion-controlled region. The XPS analysis indicates the presence of different nitrogen species. They can adjust the electronic structure of the carbon framework and facilitate O_2 adsorption and electron transfer. Furthermore, transition metal nitrides/hydroxides are known to exhibit Pt-like electronic structures, which can enhance oxygen adsorption and promote the reduction reaction. The presence of Cr–N/Cr–OH nanoparticles anchored on the NRGO sheets may provide additional catalytic sites and improve charge transfer during the ORR. In addition, the interfacial contact between the chromium-based nanoparticles and the conductive NRGO support, as observed in the TEM images, likely generates beneficial interfacial electronic interactions. Therefore, the enhanced ORR activity of the NRGO–N–CrO(OH)–C catalyst can be reasonably attributed to the combined effects of (i) nitrogen-doped graphene active sites, (ii) catalytic contributions from Cr–OH/Cr–N species, and (iii) synergistic interfacial interactions between the metal-based nanoparticles and the conductive carbon framework. These factors collectively promote efficient oxygen adsorption and facilitate a favorable four-electron ORR pathway.

The stability of NRGO, Cr_2O_3–C, NRGO–N–CrO(OH)–C, and Pt/C electrocatalysts towards the ORR was assessed *via* chronoamperometry, as depicted in Fig. 6C. After 2000 seconds, all electrocatalysts demonstrated good stability, while NRGO–N–CrO(OH)–C showing notably more stable cathodic currents, as corroborated by cyclic voltammetry findings. The resistance of NRGO–N–CrO(OH)–C to methanol was also evaluated using amperometric j–t tests as presented

in Fig. S4B. Upon adding 4 mL of methanol at 1000 seconds, the ORR current of NRGO–N–CrO(OH)–C remained stable, highlighting its high selectivity for methanol and superior methanol tolerance compared to the notable current fluctuations observed with Pt/C due to methanol oxidation.

Fig. 6D shows the Nyquist plots from electrochemical impedance spectroscopy (EIS) for different electrocatalysts at a cathodic potential of 0.8 V *vs.* RHE. As illustrated, the charge transfer resistance extracted from the semicircular diameter in the Nyquist plots for the NRGO–N–CrO(OH)–C electrocatalyst significantly decreased compared to Cr_2O_3–C and NRGO, which determines excellent electron transfer, higher conductivity, and faster kinetics for the ORR on the surface of this electrocatalyst. The corresponding equivalent circuit for the proposed electrocatalyst is illustrated in the inset of Fig. 6D, where R_s (4.1 Ω) and R_1 (4.0 Ω) represent the electrolyte resistance and charge transfer resistance of the synthesized electrocatalyst, respectively. Moreover, the corresponding equivalent circuit for NRGO shows two semicircles: a small semicircle with 59.5 Ω and a large semicircle with 22 784 Ω, demonstrating two interfacial charge transfer impedance (Fig. S5). From the fitted Nyquist plot of Cr_2O_3–C (Fig. S5), R_1 for its first semicircle was calculated to be 34.9 Ω, and the electrolyte resistance remained unchanged for all of the electrocatalysts.

The electrochemical surface areas (ECSAs) of the catalysts were also evaluated using double-layer capacitance (C_{dl}) values obtained from recorded cyclic voltammograms in the nonfaradaic region (0.95–1.15 V) (Fig. S6). Notably, the CV curve of NRGO–N–CrO(OH)–C displays a higher double-layer current than the other catalysts. The results indicate that the ECSA values for the NRGO, Cr_2O_3–C, and NRGO–N–CrO(OH)–C catalysts were 28.9, 27.1, and 36.9 cm^{-2} (or 36.8, 34.5, and 47.0 mF cm^{-2}), respectively. The incorporation of NRGO increased the ECSA, which the highest value observed for NRGO–N–CrO(OH)–C. This increase is likely due to the uniform wrapping of Cr_2O_3–C on the NRGO surface, indicating that the integration of Cr_2O_3–C with NRGO substantially enhances the ECSA. Since the ECSA is directly proportional to the redox-active sites, it is expected that NRGO–N–CrO(OH)–C may provide better ORR and supercapacitive performance compared to NRGO and Cr_2O_3–C.

It is also important to consider the potential environmental risks associated with chromium species. Although Cr(VI) compounds are known to be toxic, Cr_2O_3 (Cr^{3+}) is thermodynamically stable under alkaline ORR

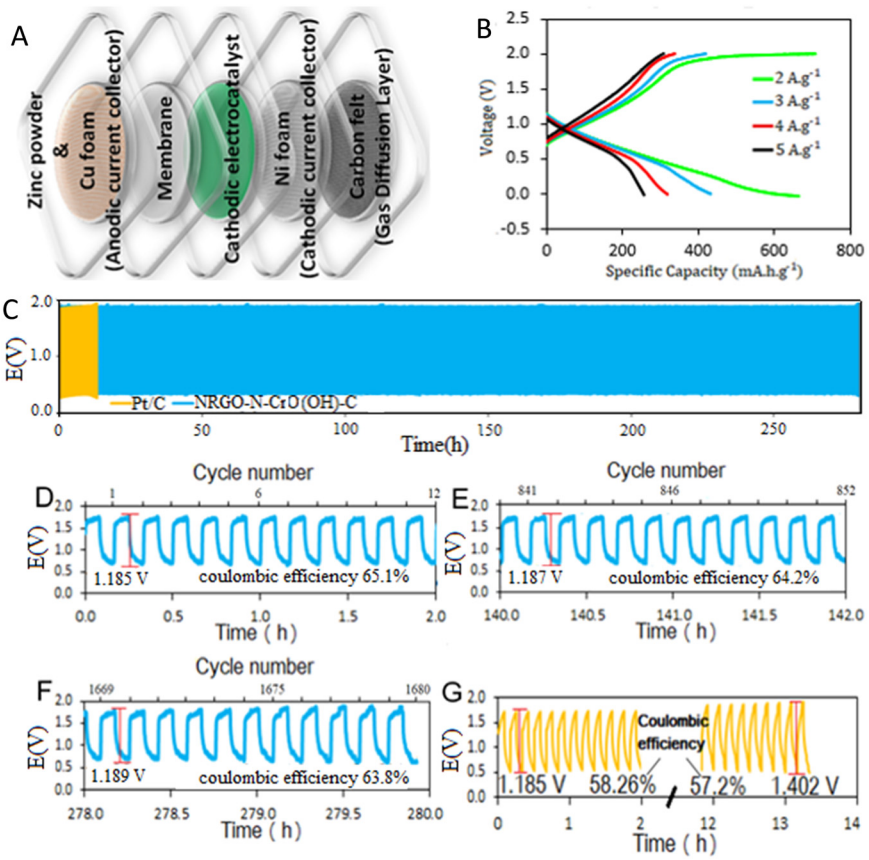

Fig. 7 (A) Schematic of the zinc–air battery, (B) charge/discharge curves at varying current densities, (C) chrono charge–discharge profile of the ZABs with NRGO–N–CrO(OH)–C and Pt/C, (D–F and G) NRGO–N–CrO(OH)–C and Pt/C ZAB round-trip efficiency and polarization voltage for different periods, respectively.

conditions. Based on the atomic absorption spectroscopy analysis, no significant performance decay related to catalyst dissolution was observed during cycling tests, suggesting structural stability of the proposed composite.

Given the outstanding electrocatalytic activity and higher active sites of NRGO–N–CrO(OH)–C for the ORR, a standard zinc–air battery was engineered to investigate the practical application of NRGO–N–CrO(OH)–C in energy storage and conversion devices.

3.3. Zn–air battery performance

The performance of the NRGO–N–CrO(OH)–C electrocatalyst in air batteries was evaluated by loading the catalyst into carbon paper at a mass loading of 1 mg cm^{-2} as the air electrode, with Zn powder and Cu foam as the anodic current collector, and a solution of 0.2 M zinc acetate and 6 M KOH as the electrolyte, as illustrated in Fig. 7A. According to the ZAB design outlined in Fig. 7A, the air electrode facilitates the oxygen reduction reaction. For comparison, a Pt/C catalyst-based ZAB was also tested under identical conditions. Fig. 7B shows the battery's discharge capacities at different current densities (2–5 A g^{-1}) with the NRGO–N–CrO(OH)–C ZAB achieving a specific capacity of 665 mA h g^{-1} at 2 A g^{-1}, showcasing competitive performance compared to reported values.[41] When cycled at a fixed current density of 2 mA cm^{-2}, the ZAB based on the NRGO–N–Cr_xO_y(OH)–C electrocatalyst delivered charge and discharge voltages of 1.79 and 0.67 V,

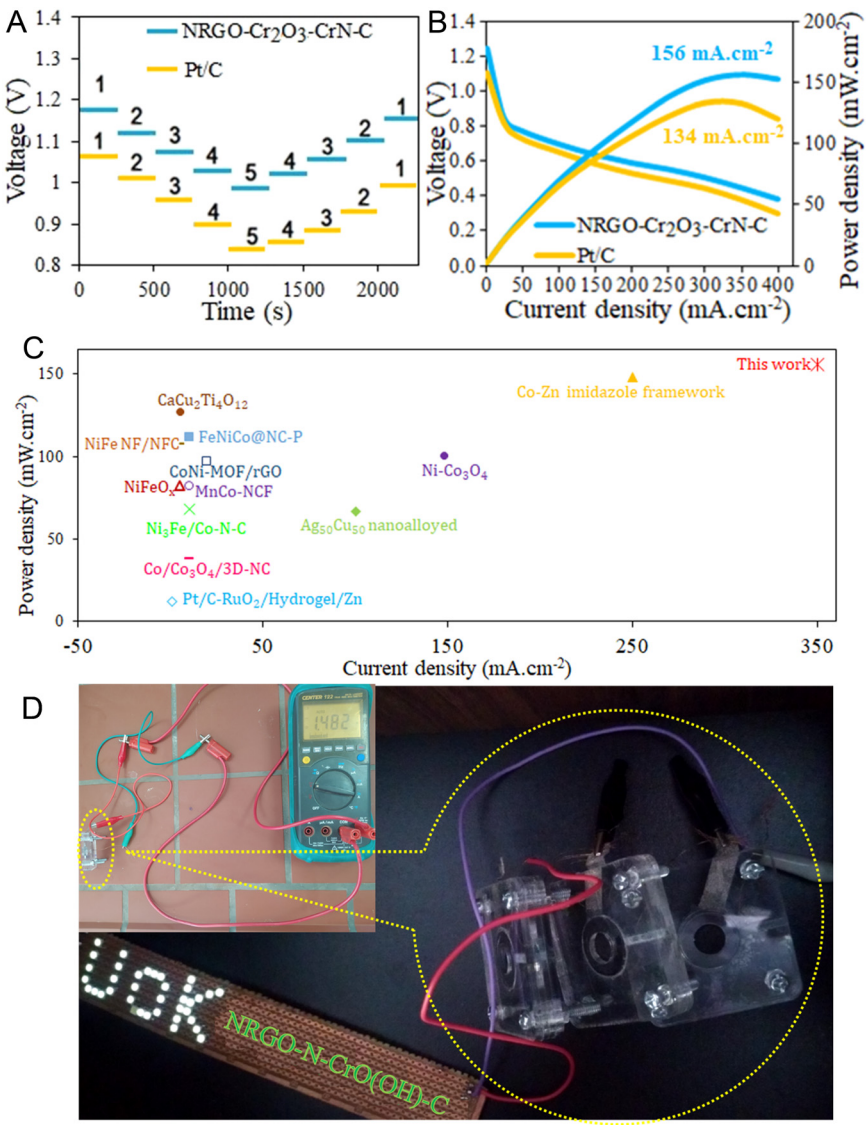

Fig. 8 (A) Comparative discharge voltages of ZABs with NRGO–N–CrO(OH)–C and Pt/C across different current densities from 1 to 5 mA cm^{-2}, (B) polarization curve (*V–j*) and corresponding power density plot of the battery using NRGO–N–CrO(OH)–C as the cathode electrocatalyst compared with the battery using the commercial Pt/C catalyst, (C) comparison of power density of different zinc ion batteries, and (D) showcasing the assembly of ZAB with surface-mounted diode (SMD) designed as UoK. Inset the proposed circuit for ZAB voltage measuring.

respectively (Fig. 7C). Notably, these voltages remained nearly stable over 280 h (1680 cycles), indicating a well rechargeability.

Fig. 7(D–F) show the coulombic efficiency and polarization voltage of the NRGO–N–CrO(OH)–C ZABs at different time intervals. The polarization voltage is 1.185 V after operating for approximately 1 h, and the coulombic efficiency reaches 65.1%. After operating for 140 h, the polarization voltage can increase to 1.187 V, and the coulombic efficiency slightly decreases to 64.2%. After 280 h of operation, the polarization voltage is still 1.189 V, and the coulombic efficiency remains at 63.8%. The polarization voltage and coulombic efficiency of Pt/C is 1.185 V and 58.3%, respectively, after operating for approximately 1 h. After operating for 13 h, the polarization voltage can increase to 1.402 V, and the coulombic efficiency slightly decreases to 57.2%, indicating the better catalytic behavior of NRGO–N–CrO(OH)–C compared to Pt/C. The plot of discharge voltage *vs.* current densities is recorded in Fig. 8A. As illustrated, the discharge voltage of the proposed Zn–air batteries exhibits a minimum decline from 1.18 V to 0.98 V with increasing current densities from 1 to 5 mA cm^{-2}, indicating the rapid mass transfer and small resistance under different current densities. Furthermore, the discharge voltage of 0.98 V is higher than that of Pt/C (0.84 V) indicating better mass transfer efficiency accompanied by high electrocatalytic activity. Compared to Pt/C, NRGO–N–CrO(OH)–C exhibited superior durability and the ability to return to its initial discharge potential, indicating excellent reversibility.

NRGO–N–CrO(OH)–C achieved a maximum current density of 350 mA cm^{-2} and a peak power density of 156 mW cm^{-2} (Fig. 8B) surpassing Pt/C and aligning with other leading electrocatalysts for ZAB cathodes.[42–53] Fig. 8C presents a comparison of the power density of this catalyst with previously reported catalysts, revealing its high performance. The NRGO–N–CrO(OH)–C catalyst-based ZAB exhibits an open-circuit voltage of 1.48 V, as shown in Fig. 8D. Additionally, all three-solid-state Zn–air batteries using the NRGO–N–CrO(OH)–C catalyst were linked in series and successfully powering several surface-mounted diode (SMD) lamps for over 10 minutes (Fig. 8D), highlighting the potential of NRGO–N–CrO(OH)–C in practical applications.

4. Conclusion

This work presents a compelling strategy for the preparation of NRGO–N–CrO(OH)–C as a highly efficient, non-Pt-based electrocatalyst for the ORR and its application as a cathode material for zinc–air batteries (ZABs). Nitrogen-doped reduced graphene oxide (NRGO) nanosheets were first synthesized *via* a simple electrochemical method using an ionic liquid electrolyte and graphite rods as electrodes. Subsequently, Cr_2O_3–C nanostructures were deposited onto the NRGO framework, followed by the formation of nitrogen-doped reduced graphene oxide-supported NRGO–N–CrO(OH)–C nanocomposites. The electrocatalytic performance of the as-prepared catalyst toward the ORR was systematically evaluated using various electrochemical techniques. The NRGO–N–CrO(OH)–C catalyst exhibited excellent ORR activity, exhibiting an onset potential of 0.86 V, a low Tafel slope of 37.7 mV dec^{-1}, and outstanding long-term stability. When employed as the air cathode in a rechargeable zinc–air battery, the NRGO–N–CrO(OH)–C catalyst achieved a high peak power density of 156 mW cm^{-2} at a current density of 350 mA cm^{-2}, a high open-circuit voltage of 1.48 V, and a specific capacity of 665 mA h g^{-1}. Moreover, the NRGO–N–CrO(OH)–C-based zinc–air battery demonstrated remarkable cycling durability, maintaining stable charge and discharge voltages of approximately 1.79 and 0.67 V, respectively, at a current density of 2 mA cm^{-2} over 1680 cycles (280 h), with a coulombic efficiency of ~63.8%. Notably, this performance surpasses commercial Pt/C catalyst, highlighting superior stability and cycle life. Collectively, these results unequivocally demonstrate that NRGO–N–CrO(OH)–C is a promising and durable ORR electrocatalyst, offering significant potential for the development of high-efficiency zinc–air batteries.

Conflicts of interest

The authors declare that they have no known competing financial interests or personal relationships that could have appeared to influence the work reported in this paper.

Data availability

The data supporting this manuscript have been included as part of the supplementary information (SI).

Supplementary information containing Fig. S1–S7 is available. See DOI: https://doi.org/10.1039/d6cy00157b.

Acknowledgements

This research was supported by the Research Office of University of Kurdistan (grant number 02-9-33926-135). In the graphical abstract, the authors acknowledge that the schematic diagram of the battery cell in the graphical abstract was generated using Google's FX Flow (ImageFX) tool *via* Google Labs.

References

1 R. Ma, G. Lin, Y. Zhou, Q. Liu, T. Zhang, G. Shan, M. Yang and J. Wang, *npj Comput. Mater.*, 2019, **5**, 78.
2 M. Keersemaker, Critical Raw materials, in *Suriname Revisited: Economic Potential of its Mineral Resources*, ed. M. Keersemaker, Springer International Publishing, Cham, 2020, pp. 69–82.
3 Z. Li, J. Li, K. Jiang, S. Yuan, D. Yu, H. Wei, Z. Shi, X. Li and H. Chu, *Chem. Eng. J.*, 2021, **411**, 128527.
4 Y. Li, Y. Wang, S. Li, M. Li, Y. Liu, X. Fang, X. Dai and X. Zhang, *J. Catal.*, 2021, **395**, 282–292.
5 S. Polani, K. E. MacArthur, J. Kang, M. Klingenhof, X. Wang, T. Möller, R. Amitrano, R. Chattot, M. Heggen, R. E. Dunin-

Borkowski and P. Strasser, *ACS Appl. Mater. Interfaces*, 2022, **14**, 29690–29702.
6 Z. Feng, Y. Ma, Y. Li, R. Li, Y. Tang and X. Dai, *Phys. Chem. Chem. Phys.*, 2020, **22**, 1493–1501.
7 K. Kakaei and A. Balavandi, *J. Colloid Interface Sci.*, 2016, **463**, 46–54.
8 K. Kakaei and A. Balavandi, *J. Colloid Interface Sci.*, 2017, **490**, 819–824.
9 X. Wang, Z. Yang, W. Si, X. Shen, X. Li, R. Li, Q. Lv, N. Wang and C. Huang, *Carbon*, 2019, **147**, 9–18.
10 H. Shen, H. Peng, R. Cao, L. Yang, Y. Gao, A. Turak, T. Thomas, X. Guo, Y. Zhu, J. Wang and M. Yang, *J. Phys. Chem. Lett.*, 2021, **12**, 517–524.
11 X.-F. Ren, Y. Liu, S.-J. Hu, D. Wu, M.-Y. Zhang, C. Wang and H. Liu, *J. Water Process Eng.*, 2024, **62**, 105366.
12 L. Cao, R. Liu, Y. Huang, D. Chu, M. Li, G. Xu, X. Li, J. Huang, Y. Zhao and L. Feng, *Molecules*, 2024, **29**, 2973.
13 S. M. Saju and A. A. Vargeese, *New J. Chem.*, 2024, **48**, 17150–17158.
14 J. Liu, Z. Luo, J. Wu, D. Qian, W. Liao, G. I. N. Waterhouse and X. Chen, *Inorg. Chem.*, 2024, **63**, 12681–12689.
15 J. S. Shaikh, M. Rittiruam, T. Saelee, V. Márquez, N. S. Shaikh, P. Khajondetchairit, S. Pathan, P. Kanjanaboos, T. Taniike, M. K. Nazeeruddin, P. Praserthdam and S. Praserthdam, *Mater. Sci. Eng., R*, 2024, **160**, 100813.
16 Y. Xue, Y. Wang, Z. Zheng, Q. Lu, W. Chen, S. Yan, S. Sun, H. Zhang and G. Shao, *J. Electroanal. Chem.*, 2024, **963**, 118329.
17 K. S. Smith, C. Adjah-Tetteh, Z. He, G. Yang, Y. Wang, S. Bliznakov, R. Maric, N. Xu and X.-D. Zhou, *J. Phys. Chem. C*, 2025, **129**, 16507–16515.
18 N. Xu, Y. Liu, X. Zhang, X. Li, A. Li, J. Qiao and J. Zhang, *Sci. Rep.*, 2016, **6**, 33590.
19 Z. He, N. Xu, Y. Wang, D. Chao, R. Maric, A. Virkar and X.-D. Zhou, *Chem. Eng. J.*, 2026, **527**, 171444.
20 L. M. Rivera, G. García and E. Pastor, *Curr. Opin. Electrochem.*, 2018, **9**, 233–239.
21 J. Lilloja, E. Kibena-Põldsepp, M. Merisalu, P. Rauwel, L. Matisen, A. Niilisk, E. S. F. Cardoso, G. Maia, V. Sammelselg and K. Tammeveski, *Catalysts*, 2016, **6**(7), 108.
22 A. Sarapuu, E. Kibena-Põldsepp, M. Borghei and K. Tammeveski, *J. Mater. Chem. A*, 2018, **6**, 776–804.
23 Y. Liao, H. Chen, C. Ou, L. Bao, R. Li and H. Liu, *J. Electroanal. Chem.*, 2022, **921**, 116560.
24 A. Navaee and A. Salimi, *RSC Adv.*, 2015, **5**(74), 59874–59880.
25 W. Si, Z. Yang, X. Wang, Q. Lv, F. Zhao, X. Li, J. He, Y. Long, J. Gao and C. Huang, *ChemSusChem*, 2019, **12**, 173–178.
26 X. Zhang, X. Zhang, X. Xiang, C. Pan, Q. Meng, C. Hao, Z. Qun Tian, P. Kang Shen and S. Ping Jiang, *ChemElectroChem*, 2021, **8**, 3262–3272.
27 J. Hu, H. Li and X. Huang, *Electrochem. Solid-State Lett.*, 2005, **8**, A66.
28 B. Guo, M. Chi, X.-G. Sun and S. Dai, *J. Power Sources*, 2012, **205**, 495–499.
29 L. Dupont, S. Laruelle, S. Grugeon, C. Dickinson, W. Zhou and J.-M. Tarascon, *J. Power Sources*, 2008, **175**, 502–509.
30 C. Liang, M. Gao, H. Pan, Y. Liu and M. Yan, *J. Alloys Compd.*, 2013, **575**, 246–256.
31 H. Liu, S. Zhu, Z. Cui, Z. Li, S. Wu and Y. Liang, *J. Catal.*, 2021, **396**, 402–408.
32 N. Sadeghi, A. Khorshidi and M. Ganjali, *Inorg. Chem. Commun.*, 2021, **126**, 108489.
33 S. M. Abbas, N. Ahmad, A. ur-Rehman, U. A. Rana, S. U.-D. Khan, S. Hussain and K.-W. Nam, *Electrochim. Acta*, 2016, **212**, 260–269.
34 Y. Zhao, J. Wang, C. Ma and Y. Li, *Chem. Phys. Lett.*, 2018, **704**, 31–36.
35 J. Fu, Z. P. Cano, M. G. Park, A. Yu, M. Fowler and Z. Chen, *Adv. Mater.*, 2017, **29**, 1604685.
36 S. Peng, *Zinc–Air Batteries: Fundamentals, Key Materials and Application*, Springer Nature Singapore, Singapore, 2023.
37 K. Kakaei and M. Rahnavardi, *Renewable Energy*, 2021, **163**, 1277–1286.
38 H. Xu, M. Zeng and J. Li, *Int. J. Electrochem. Sci.*, 2015, **10**, 7361–7370.
39 L. G. Caṇado, K. Takai, T. Enoki, M. Endo, Y. A. Kim, H. Mizusaki, A. Jorio, L. N. Coelho, R. Magalhães-Paniago and M. A. Pimenta, *Appl. Phys. Lett.*, 2006, **88**, 163106.
40 I. Shafi, E. Liang and B. Li, *J. Alloys Compd.*, 2021, **851**, 156046.
41 B. T. Sone, E. Manikandan, A. Gurib-Fakim and M. Maaza, *Green Chem. Lett. Rev.*, 2016, **9**, 85–90.
42 J. Tan, T. Thomas, J. Liu, L. Yang, L. Pan, R. Cao, H. Shen, J. Wang, J. Liu and M. Yang, *Chem. Eng. J.*, 2020, **395**, 125151.
43 X. Zheng, Y. Cao, D. Liu, M. Cai, J. Ding, X. Liu, J. Wang, W. Hu and C. Zhong, *ACS Appl. Mater. Interfaces*, 2019, **11**, 15662–15669.
44 D. Zheng, W. Liu, X. Dai, J. Feng, X. Xu, R. Yin, W. Que, W. Shi, F. Wu, H. Wu and X. Cao, *Adv. Energy Sustainability Res.*, 2022, **3**, 2200014.
45 Y. Jiang, Y.-P. Deng, R. Liang, J. Fu, R. Gao, D. Luo, Z. Bai, Y. Hu, A. Yu and Z. Chen, *Nat. Commun.*, 2020, **11**, 5858.
46 U. Bhardwaj, A. Sharma, V. Gupta, K. M. Batoo, S. Hussain and H. S. Kushwaha, *Sci. Rep.*, 2022, **12**, 3999.
47 C. Lin, S. S. Shinde, Y. Wang, Y. Sun, S. Chen, H. Zhang, X. Li and J.-H. Lee, *Sustainable Energy Fuels*, 2017, **1**, 1909–1914.
48 X. Chen, L. Wei, Y. Wang, S. Zhai, Z. Chen, S. Tan, Z. Zhou, A. K. Ng, X. Liao and Y. Chen, *Energy Storage Mater.*, 2018, **11**, 134–143.
49 J. H. Park, J.-H. Shin, J.-M. Ju, J.-H. Lee, C. Choi, Y. So, H. Lee and J.-H. Kim, *Nano Convergence*, 2022, **9**, 17.
50 Y. Lei, F. Chen, Y. Jin and Z. Liu, *Nanoscale Res. Lett.*, 2015, **10**, 197.
51 R. Chen, X. Xu, S. Peng, J. Chen, D. Yu, C. Xiao, Y. Li, Y. Chen, X. Hu, M. Liu, H. Yang, I. Wyman and X. Wu, *ACS Sustainable Chem. Eng.*, 2020, **8**, 11501–11511.
52 G. Li, M. A. Mezaal, K. Zhang and L. Lei, *Int. J. Electrochem. Sci.*, 2015, **10**, 5395–5404.

53 D. Ren, J. Ying, M. Xiao, Y.-P. Den, J. Ou, J. Zhu, G. Liu, Y. Pei, S. Li, A. M. Jauhar, H. Jin, S. Wang, D. Su, A. Yu and Z. Chen, *Adv. Funct. Mater.*, 2019, **30**, 1908167.
54 P. Singh and D. A. Buttry, *J. Phys. Chem. C*, 2012, **116**, 10656–10663.
55 A. J. Bard and L. R. Faulkner, Electrochemical Methods, Wiley, New York, 1980.
56 K. Szwabińska and G. Lota, *Electrochem. Commun.*, 2022, **141**, 107359.